CrossMark

Refined Mass and Geometric Measurements of the High-mass PSR J0740+6620

E. Fonseca[1,2,3,4], H. T. Cromartie[5,37], T. T. Pennucci[6,7], P. S. Ray[8], A. Yu. Kirichenko[9,10], S. M. Ransom[6],
P. B. Demorest[11], I. H. Stairs[12], Z. Arzoumanian[13], L. Guillemot[14,15], A. Parthasarathy[16], M. Kerr[8], I. Cognard[14,15],
P. T. Baker[17], H. Blumer[3,4], P. R. Brook[3,4], M. DeCesar[18], T. Dolch[19,20], F. A. Dong[12], E. C. Ferrara[21,22,23],
W. Fiore[3,4], N. Garver-Daniels[3,4], D. C. Good[12], R. Jennings[24], M. L. Jones[25], V. M. Kaspi[1,2], M. T. Lam[26,27],
D. R. Lorimer[3,4], J. Luo[28], A. McEwen[25], J. W. McKee[28], M. A. McLaughlin[3,4], N. McMann[29], B. W. Meyers[12],
A. Naidu[30], C. Ng[31], D. J. Nice[32], N. Pol[29], H. A. Radovan[33], B. Shapiro-Albert[3,4], C. M. Tan[1,2],
S. P. Tendulkar[34,35], J. K. Swiggum[32], H. M. Wahl[3,4], and W. W. Zhu[36]

[1] Department of Physics, McGill University, 3600 rue University, Montréal, QC H3A 2T8, Canada
[2] McGill Space Institute, McGill University, 3550 rue University, Montréal, QC H3A 2A7, Canada
[3] Department of Physics and Astronomy, West Virginia University, Morgantown, WV 26506-6315, USA
[4] Center for Gravitational Waves and Cosmology, Chestnut Ridge Research Building, Morgantown, WV 26505, USA
[5] Cornell Center for Astrophysics and Planetary Science and Department of Astronomy, Cornell University, Ithaca, NY 14853, USA
[6] National Radio Astronomy Observatory, 520 Edgemont Road, Charlottesville, VA 22903, USA
[7] Institute of Physics, Eötvös Lorán University, Pázmány P.s. 1/A, 1117 Budapest, Hungary
[8] U.S. Naval Research Laboratory, Washington, DC 20375, USA
[9] Universidad Nacional Autónoma de México, Instituto de Astronomía, AP 106, Ensenada 22800, BC, México
[10] Ioffe Institute, Politekhnicheskaya 26, St. Petersburg, 194021, Russia
[11] National Radio Astronomy Observatory, P.O. Box O, Socorro, NM 87801, USA
[12] Department of Physics & Astronomy, University of British Columbia, 6224 Agricultural Road, Vancouver, BC V6T 1Z1, Canada
[13] Astrophysics Science Division, Code 662, NASA Goddard Space Flight Center, Greenbelt, MD 20771, USA
[14] Laboratoire de Physique et Chimie de l'Environnement et de l'Espace—Université d'Orléans / CNRS, F-45071 Orléans Cedex 02, France
[15] Station de radioastronomie de Nançay, Observatoire de Paris, CNRS/INSU, F-18330 Nançay, France
[16] Max Planck Institute for Radio Astronomy, Auf dem Hügel 69, D-53121 Bonn, Germany
[17] Department of Physics and Astronomy, Widener University, Chester, PA 19013, USA
[18] Department of Physics and Astronomy, George Mason University, Fairfax, VA 22030, resident at U.S. Naval Research Laboratory, Washington, D.C. 20375, USA
[19] Department of Physics, Hillsdale College, 33 E. College Street, Hillsdale, MI 49242, USA
[20] Eureka Scientific, Inc. 2452 Delmer Street, Suite 100, Oakland, CA 94602-3017, USA
[21] Department of Astronomy, University of Maryland, College Park, MD 20742, USA
[22] Center for Exploration and Space Studies (CRESST), USA
[23] NASA Goddard Space Flight Center, Greenbelt, MD 20771, USA
[24] Department of Astronomy, Cornell University, Ithaca, NY 14853, USA
[25] Center for Gravitation, Cosmology, and Astrophysics, Department of Physics, University of Wisconsin-Milwaukee, P.O. Box 413, Milwaukee, WI 53201, USA
[26] School of Physics and Astronomy, Rochester Institute of Technology, Rochester, NY 14623, USA
[27] Laboratory for Multiwavelength Astrophysics, Rochester Institute of Technology, Rochester, NY 14623, USA
[28] Canadian Institute for Theoretical Astrophysics, University of Toronto, 60 St. George Street, Toronto, ON M5S 3H8, Canada
[29] Department of Physics and Astronomy, Vanderbilt University, 2301 Vanderbilt Place, Nashville, TN 37235, USA
[30] University of Oxford, Sub-Department of Astrophysics, Denys Wilkinson Building, Keble Road, Oxford, OX1 3RH, UK
[31] Dunlap Institute for Astronomy & Astrophysics, University of Toronto, 50 St. George Street, Toronto, ON M5S 3H4, Canada
[32] Department of Physics, Lafayette College, Easton, PA 18042, USA
[33] Department of Physics, University of Puerto Rico, Mayagüez, PR 00681, USA
[34] Department of Astronomy and Astrophysics, Tata Institute of Fundamental Research, Mumbai, 400005, India
[35] National Centre for Radio Astrophysics, Post Bag 3, Ganeshkhind, Pune, 411007, India
[36] National Astronomical Observatories, Chinese Academy of Sciences, Beijing 100101, People's Republic of China; efonseca@physics.mcgill.ca

Abstract

We report results from continued timing observations of PSR J0740+6620, a high-mass, 2.8 ms radio pulsar in orbit with a likely ultracool white dwarf companion. Our data set consists of combined pulse arrival-time measurements made with the 100 m Green Bank Telescope and the Canadian Hydrogen Intensity Mapping Experiment telescope. We explore the significance of timing-based phenomena arising from general relativistic dynamics and variations in pulse dispersion. When using various statistical methods, we find that combining ~1.5 yr of additional, high-cadence timing data with previous measurements confirms and improves on previous estimates of relativistic effects within the PSR J0740+6620 system, with the pulsar mass $m_p = 2.08^{+0.07}_{-0.07} M_\odot$ (68.3% credibility) determined by the relativistic Shapiro time delay. For the first time, we measure secular variation in the orbital period and argue that this effect arises from apparent acceleration due to significant transverse motion. After incorporating contributions from Galactic differential rotation and off-plane acceleration in the Galactic potential, we obtain a model-dependent distance of $d = 1.14^{+0.17}_{-0.15}$ kpc (68.3% credibility). This improved distance confirms the ultracool nature of the white dwarf companion determined from recent optical observations. We discuss the prospects for future observations with next-generation facilities, which will likely improve the precision on m_p for J0740+6620 by an order of magnitude within the next few years.

[37] NASA Hubble Fellowship Program Einstein Postdoctoral Fellow.

1

1. Introduction

The masses and radii of neutron stars are a central focus in many observational high-energy experiments. Members of the neutron star population with the largest masses are particularly important. A key application of these measurements is in testing proposed neutron star equations of state (EOSs), of which there are many that incorporate baryonic and/or "exotic" compositions not accessible through terrestrial experiments (Özel & Freire 2016). For many decades, the primary means of measuring precise neutron star masses was through timing of radio pulsars in orbital systems that exhibit relativistic dynamical processes (e.g., Stairs 2003). Observatories sensitive to X-ray and gravitational radiation have begun to yield similar estimates of masses and radii, propelling statistical inference of fundamental physics and EOS constraints from neutron stars into a new and exciting era (e.g., Abbott et al. 2018; Miller et al. 2019; Riley et al. 2019).

A recent example of important observational constraints arises from the timing of PSR J0740+6620, a 2.8 ms millisecond pulsar (MSP) in a near-circular, 4.7-day orbit discovered by the Green Bank North Celestial Cap Survey (Lynch et al. 2018). Measurement of the relativistic Shapiro time delay (Shapiro 1964) in the PSR J0740+6620 system allowed for an estimate of the pulsar mass, $m_p = 2.14^{+0.10}_{-0.09}\,M_\odot$ (68.3% credibility; Cromartie et al. 2020). An optical search for the white dwarf companion to PSR J0740+6620 yielded a detection of a likely ultracool counterpart (Beronya et al. 2019), though a firm association is dependent on a reliable measure of distance that was not obtainable at the time. These radio and optical-photometric data were shown to be consistent with binary stellar evolution simulations of a progenitor system undergoing conservative mass transfer within a Hubble time, regardless of whether irradiation feedback was prominent in system evolution (Echeveste et al. 2020).

Along with PSRs J0348+0423 (Antoniadis et al. 2013) and J1614−2230 (e.g., Demorest et al. 2010), PSR J0740+6620 resides at the high-mass extremum of the known Galactic pulsar population. In addition, and while subject to greater modeling uncertainty, observations of "redback" pulsars and their irradiated companions clearly suggest a substantial population of high-mass neutron stars (e.g., van Kerkwijk et al. 2011; Linares et al. 2018; Romani et al. 2021). Gravitational-wave observations of GW190814 indicate a high-mass compact object that could be the heaviest neutron star known (Abbott et al. 2020). A small yet growing population, high-mass neutron stars serve as the most important constraints on the maximum allowed masses and, by extension, the EOS models that predict these measurements (e.g., Hu et al. 2020; Raaijmakers et al. 2020; Tsokaros et al. 2020). Further study of the high-mass pulsar population will also allow for an ensemble estimation of the maximum mass, as well as the study of distribution moments that reflect underlying formation processes, before or during the spin-up to millisecond rotational periods, that produce high-mass neutron stars (e.g., Antoniadis et al. 2016).

Recently, the Neutron Star Interior Composition Explorer (NICER) measured the mass and radius of the isolated PSR J0030+0451 through modeling of X-ray thermal emission from hot spots on the neutron star surface (Bogdanov et al. 2019; Miller et al. 2019; Raaijmakers et al. 2019; Riley et al. 2019). Constraints on neutron star radii from NICER observations are strengthened with a priori knowledge of their masses. For sufficiently bright pulsars in binary systems, typically with system inclination $i \gtrsim 60°$, mass and geometric measurements can be achieved with high-precision pulsar timing. In late 2019, NICER confirmed X-ray pulsations from PSR J0740+6620 (Wolff et al. 2021) and began a dedicated observing program to infer the stellar compactness via modeling of its pulsed X-ray emission. We endeavor to improve on the mass measurement of Cromartie et al. (2020) and constrain other physical parameters in support of NICER observations and their constraints on the radius.

In this work, we present observations, analysis, and results from ongoing timing observations of PSR J0740+6620 with two different telescopes. In Section 2, we overview the instruments and processing methods used to acquire pulse arrival-time data for PSR J0740+6620. In Section 3, we describe the procedure used to simultaneously model arrival times obtained with different instruments and receivers. In Section 4, we outline the theoretical framework used in order to obtain robust constraints on the Shapiro delay and distance to PSR J0740+6620. In Section 5, we discuss various aspects of our analysis and results, including dispersion measure (DM) modeling and impacts our measurements have on recent optical observations. Finally, in Section 6, we summarize our results and speculate about future improvement of our measurements.

2. Observations and Reduction

Continued observations of PSR J0740+6620 were conducted using the 100 m Green Bank Telescope (GBT) and the Canadian Hydrogen Intensity Mapping Experiment (CHIME) telescope. A summary of observing parameters and statistics is presented in Table 1.

2.1. Telescopes

Nearly all data from the single-dish GBT were acquired as part of the ongoing observing program of the North American Nanohertz Observatory for Gravitational Waves (NANOGrav),[38] which monitors an array of nearly 100 MSPs for signatures of gravitational radiation at nanohertz frequencies. Details of the NANOGrav observing program are given by Alam et al. (2021a, 2021b), and we provide a summary here.

At the GBT, raw telescope voltage data were coherently dedispersed and processed in real time through the Green Bank Ultimate Pulsar Processing Instrument (GUPPI; DuPlain et al. 2008). During its operation, GUPPI produced archives of time-integrated (or "folded") pulse profiles, and for all elements of the Stokes polarization vector, over 10 s time bins. Folded profiles were collected using two different radio receivers at the GBT, with the receivers centered at radio frequencies of 820 and 1400 MHz; these receivers possessed full bandwidths of 200 and 800 MHz, respectively. Moreover, the spectrum of each folded profile was resolved over 128 and 512 channels when using the 820 and 1400 MHz receivers, respectively.

---

[38] nanograv.org

Table 1
Summary of Observing Parameters and Data Sets of PSR J0740+6620 Analyzed in This Work

Parameter	GBT/1400 MHz	GBT/820 MHz	CHIME
Time range (MJD)	56,675–58,945	56,640–58,944	58,517–58,975
Frequency range (MHz)	1151–1885	722–919	400–800
Number of channels, raw	512	128	1024
Number of channels, downsampled	64	64	32
Number of observing epochs	187	142	263
Number of TOAs, narrowband	8208	5191	4862
Number of TOAs, wideband	209	154	263
Min./median/max. σ_{TOA}, narrowband (μs)	0.24/2.65/32.7	0.16/3.16/24.9	0.49/5.21/62.8
Min./median/max. σ_{TOA}, wideband (μs)	0.05/0.39/2.04	0.04/0.51/3.10	0.14/0.97/3.28

The GBT data set analyzed in this work also contains supplemental observations acquired by Cromartie et al. (2020) near and during superior conjunction in the PSR J0740+6620 binary system. Targeted observations have been shown to increase the measurement significance of the Shapiro time delay, which is at its maximum amplitude during superior conjunction (orbital phase of 0.25, relative to the ascending node; e.g., Demorest et al. 2010; Pennucci 2015). The targeted observations of PSR J0740+6620 occurred over three sessions: one 6 hr session occurred on MJD 58368 using the 820 MHz receiver during orbital phase of 0.25, and two 5 hr sessions were undertaken on MJDs 58448 and 58449 using the 1400 MHz receiver, corresponding to orbital phases of 0.15 and 0.25, respectively.

The CHIME telescope is a static radio interferometer composed of four half-cylinder reflectors and a total of 1024 dual-polarization antennas sensitive to the 400–800 MHz range. Digitized telescope voltage data from all CHIME feeds are coherently averaged using time-dependent phase delays corresponding to 10 different sources, instantaneously yielding 10 "tracking" voltage time series. The CHIME/Pulsar back end (CHIME/Pulsar Collaboration et al. 2020) is a 10-node computing system that receives these 10 independent, complex voltage streams—at resolutions of 2.56 μs and 1024 frequency channels—and uses dspsr (van Straten & Bailes 2011) to perform real-time coherent dedispersion and folding. The resultant products are similar in structure to those acquired with GUPPI, though they contain 1024 channels evaluated across the 400 MHz bandwidth of CHIME for each recorded profile. At the decl. of PSR J0740+6620, acquisitions typically occur with a duration of ∼33 minutes in order to record a full transit at the CHIME telescope.

2.2. Observing Cadences

Under the nominal NANOGrav program, multifrequency observations of PSR J0740+6620 with the GBT typically lasted for ∼25 minutes per receiver and occurred with a monthly cadence; observations with each receiver were acquired within ∼3 days of one another. After 2018 September 24 (i.e., MJD 58385), observations of PSR J0740+6620 were prioritized to occur during every scheduled NANOGrav session, which led to three to five multifrequency observations within a 1-week period of time during each month. See Alam et al. (2021a, 2021b) for additional discussion on the NANOGrav observing program.

Folded data were acquired with the CHIME/Pulsar coherent-dedispersion back end on a near-daily basis from 2019 February 3 to 2020 May 6 (i.e., MJD range 58517–58975).

Exceptions to the near-daily cadence largely correspond to ∼1-week periods where the CHIME correlator ceased operation for software upgrades and hardware maintenance. Such activities only occurred three to four times per year during the time span of CHIME data presented in this work.

2.3. Offline Processing, Calibration, and Downsampling

All data acquired with the GBT and CHIME/Pulsar were processed offline using the psrchive[39] suite of analysis utilities, through the use of separate psrchive-based procedures tailored to the NANOGrav and CHIME/Pulsar data sets. For NANOGrav data on PSR J0740+6620, we used the nanopipe pipeline[40]—which is employed in ongoing NANOGrav analysis of all its sources—for the following manipulations: mask-based excision of radio frequency interference (RFI), calibration of flux density and polarization information using on/off-source observations of the compact radio source J1445+0958 (B1442+101) modulated with a pulsed noise diode, downsampling to frequency resolution as low as 3.125 MHz per channel, and full integration of profiles across the duration of each scan.

CHIME/Pulsar data were processed using a similar procedure, but with three modifications: (1) the Stokes profiles were not calibrated owing to ongoing work in developing calibration methods for CHIME/Pulsar data; (2) spectra were downsampled to 32 channels with 12.5 MHz bandwidth, in order to retain adequate signal-to-noise ratio (S/N) in as many channels as possible; and (3) ∼1 minute of profile data acquired before and after the transit of PSR J0740+6620 at CHIME was discarded prior to integration of profile data over time. The third modification was performed in order to minimize overweighting of CHIME/Pulsar profiles recorded at low frequencies, where the primary beam of CHIME is wider and is thus sensitive to transiting pulsars for longer periods of time.

2.4. Computation of Arrival Times

We generated two distinct sets of times of arrival (TOAs) and TOA uncertainties (σ_{TOA}) from processed GBT and CHIME/Pulsar data: a set of frequency-resolved TOAs, which we refer to as "narrowband" TOAs, and a set of "wideband" TOAs, which extract a single arrival-time measurement from each observation.

The narrowband TOAs were measured using the Fourier phase-gradient technique described in Taylor (1992); the

---

[39] http://psrchive.sourceforge.net/
[40] https://github.com/demorest/nanopipe

observed total-intensity (i.e., Stokes I) profile from each frequency channel is cross-correlated with a de-noised template to measure a best-fit phase offset. The template profile is constructed for each telescope and receiver combination by averaging all available per-receiver timing data and then wavelet-smoothing the result (e.g., NANOGrav Collaboration et al. 2015). These techniques of template and TOA generation form a standard protocol in pulsar astronomy and were employed by Cromartie et al. (2020) in their analysis of the PSR J0740+6620 system.

In this work, we obtained a maximum of 64 narrowband TOAs for each receiver bandwidth and all processed, RFI-cleaned observations. Narrowband TOAs derived from GBT data were further cleaned by removing outlier timing data using the NANOGrav analysis procedure outlined by Alam et al. (2021a), where TOAs were discarded from analysis based on low profile fidelity (i.e., with a pulse profile $S/N < 8$), corrupted calibration data, a probabilistic classification of outlier TOAs based on prior timing models (Vallisneri & van Haasteren 2017), and manual TOA excision. Narrowband TOAs derived from CHIME/Pulsar data were cleaned using a similar procedure, though this only consisted of rejecting low-S/N profiles and performing small amounts of manual TOA excision. Work is underway to fully integrate CHIME/Pulsar data into the NANOGrav analysis infrastructure and will be presented in future analyses.

Wideband TOAs are a more recent innovation (Liu et al. 2014; Pennucci et al. 2014; Pennucci 2019) but have been incorporated in the recently released 12.5 yr NANOGrav data set (Alam et al. 2021b). The wideband TOAs used for our analysis were generated using the procedure described by Pennucci et al. (2014),[41] which we briefly summarize as follows. A single, wideband TOA and instantaneous DM were estimated for each observation using a generalized Fourier phase-gradient algorithm that constrains the frequency-dependent (FD) phase offsets. In order to derive a "portrait" template for each receiver band, we first integrated all available data and computed a high-S/N template; the three mean portraits are conjoined and shown in Figure 1. The de-noised portraits, computed for each receiver band from the averaged templates, were then derived through a combination of principal component analysis, wavelet smoothing, and spline interpolation. The only TOAs excised from the wideband data set were those from low-S/N observations (with $S/N < 25$; see Alam et al. 2021b, for further explanation).

3. Timing Methods

We constructed separate models of timing variations in PSR J0740+6620 using the narrowband and wideband data sets described in Section 2.4. For each TOA set, we combined NANOGrav and CHIME/Pulsar TOAs and used the `tempo` pulsar timing package[42] for conversion and generalized least-squares modeling (Coles et al. 2011) in terms of parameters that are specific to relevant physical processes and instrumental effects. A summary of the timing procedure and model is provided below.
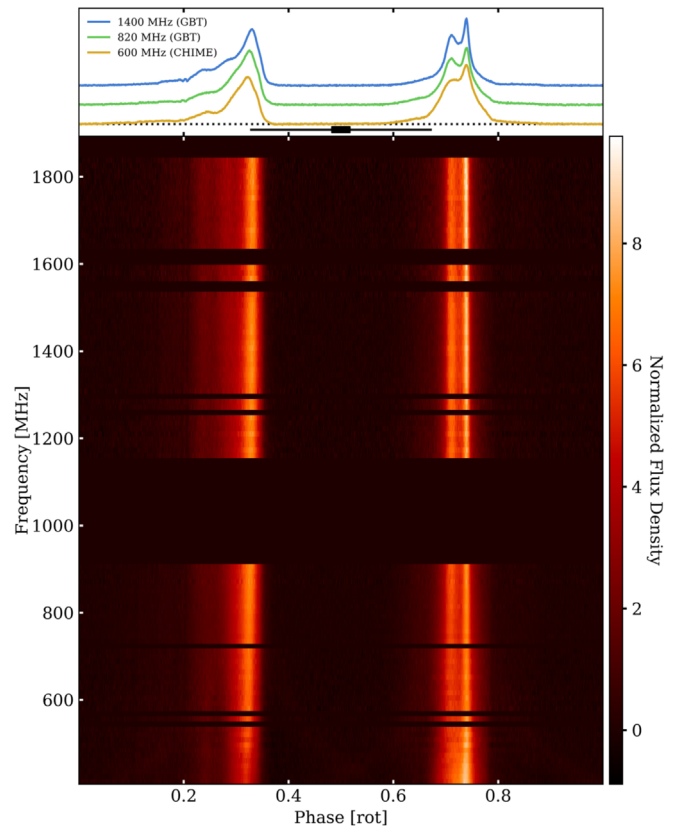

Figure 1. A composite spectrum of mean pulse profiles for PSR J0740+6620 across the three observed CHIME and GBT bands (Table 1). For each receiver, we integrated all data across observing time and downsampled in frequency and phase to match the CHIME/Pulsar resolution (12.5 MHz channels, 1024 phase bins). The amplitudes of each profile are scaled such that all profiles have unit integrated flux density. The profiles from each distinct band have been aligned for display against an arbitrary template of fixed Gaussian components, and the frequency-averaged profile from each band is displayed in the top panel. The horizontal line and bar in the top panel both denote timescale, with the line spanning 1 ms and the bar spanning 100 μs. The large gap around 1000 MHz is the gap between the GBT bands, and the narrow gap around 720 MHz exists because the upper 20% of the CHIME band was excised for this plot. Other small gaps are places where there was persistent RFI or band roll-off.

3.1. Pre-modeling Conversion of TOAs

For the CHIME/Pulsar data set, a small portion of the earliest TOAs were impacted by timing offsets that occurred upon restarts of the CHIME correlator. These offsets arose as a result of improper packaging of timing data required for downstream, real-time processing and determination of UTC time stamps. The relevant correlator software was amended to resolve this error, and all CHIME/Pulsar data acquired after MJD 58600 no longer contain achromatic timing offsets between observing cycles. We used configuration metadata recorded by the CHIME software infrastructure to determine the exact time steps introduced by two correlator offsets, and we used those values as corrections to data acquired between MJDs 58517–58543.[43]

3.2. Construction of the Timing Model

The barycentric TOAs were then modeled against a super-position of analytic time delays describing various effects of physical and instrumental origin (e.g., Backer & Hellings 1986). Parameters of these time delays consist of terms describing pulsar spin and its spin-down evolution; astrometric effects, which yield measures of position, proper motion, and apparent variations of position due to timing parallax (ϖ); piecewise-constant estimates of DM across the time span of the combined data set, referred to below as "DMX"; and orbital motion.

We used the ELL1 binary timing model (Lange et al. 2001) to model the near-circular Keplerian motion of PSR J0740 +6620 in its orbit with the companion white dwarf. The five Keplerian elements in our model consist of the orbital period (P_b); the projected semimajor axis along the line of sight (x); the epoch of passage through the ascending node of the binary system (T_{asc}); and the "Laplace-Lagrange" eccentricity parameters, ϵ_1 and ϵ_2, that describe departures from circular motion. The ELL1 parameters are related to the traditional orbital elements—eccentricity (e), argument of periastron (ω), and epoch of passage through periastron (T_0)—in the following manner:

$$e = \sqrt{\epsilon_1^2 + \epsilon_2^2} \qquad (1)$$

$$\omega = \arctan(\epsilon_1/\epsilon_2) \qquad (2)$$

$$T_0 = T_{\mathrm{asc}} + P_b \times \omega/(2\pi). \qquad (3)$$

Following Cromartie et al. (2020), we also included the Shapiro delay in our modeling of the extended data set, described by the "range" (r) and "shape" (s) parameters. While $s = \sin i$, where i is the inclination of the binary system relative to the plane of the sky, the exact expression of r depends on the assumed theory of gravitation (Damour & Taylor 1992); we assumed that general relativity is valid at the level of timing precision achieved in this work, which leads to $r = T_\odot m_c$, where $T_\odot = GM_\odot/c^{-3} = 4.925490947\ \mu$s and m_c is the mass of the companion star. With estimates of m_c and $\sin i$, the pulsar mass (m_p) is determined by the Keplerian mass function,

$$f_m = \frac{4\pi^2}{T_\odot}\frac{x^3}{P_b^2} = \frac{(m_c \sin i)^3}{(m_p + m_c)^2}. \qquad (4)$$

The significance of all model parameters was determined using the F-test criterion, as described in Alam et al. (2021a) for standard NANOGrav analysis, when comparing best-fit models that included or ignored each relevant set of parameters. We chose a p-value threshold of 0.0027 to reject the null hypothesis that adding or removing a parameter results in a variation of the residuals consistent with noise. Under Gaussian interpretation, a threshold of 0.0027 corresponds to a 3σ deviation. Parameters were included in the model if their inclusion resulted in rejection of the null hypothesis based on this test. We explored fitting for secular variations in the orbital elements using the F-test criterion and found that the time derivative of the orbital period ($\dot{P}_b$) possessed sufficient statistical significance for inclusion as a degree of freedom. We interpret and discuss the implications of the $\dot{P}_b$ measurement in several sections below.

3.3. Frequency Evolution of Pulse Profiles

One of the key differences between the commonly used narrowband methods of TOA estimation and wideband TOA estimation is their treatment of intrinsic profile evolution across receiver bandpasses. A single, achromatic template profile is used to measure our narrowband TOAs. Systematic time delays arise in the TOAs as a function of frequency in the presence of significant variation of the profile shape, which can be seen in Figure 1. We modeled these FD variations in our narrowband TOA data set using the heuristic model developed by NANOGrav Collaboration et al. (2015), where the associated time delay $\Delta t_{\mathrm{FD}} = \sum_{i=1}^{n} c_i \ln(f/1\mathrm{GHz})^i$. The coefficients c_i are free parameters in tempo, and we included three FD coefficients—with the number of coefficients determined using the F-test procedure described above—in all timing models derived from narrowband TOAs.

For the wideband TOAs, the use of a high-fidelity FD template ameliorates the timing biases introduced by profile evolution. The FD parameters were not significant when checked by the F-test. However, it is necessary to include three timing model parameters that quantify an offset in the average DM measured in each receiver band due to template profile misalignment; these DM parameters are analogous to the common phase "JUMP" parameters in tempo (see the "DMJUMP" parameters described in Alam et al. 2021b).

3.4. Analysis of Noise Properties

A common procedure in pulsar timing is the analysis of noise properties in TOA residuals (the differences between measured TOAs and their values predicted by the best-fit timing model). This type of analysis involves using a number of heuristic parameters such that the uncertainty-normalized residuals are normally distributed with unit variance. One set of these parameters adjusts the TOA uncertainties by a multiplicative factor (F_k), and a second set of these parameters is added to the TOA uncertainties in quadrature (Q_k). The subscript k denotes the unique data subset for a set of front-end/back-end combinations and corresponds to the three subsets presented in Table 1 for this work. The factor F_k accounts for incorrect estimation of σ_{TOA} due to mismatch between the data and template profiles, while Q_k characterizes underlying additive white noise (i.e., statistical fluctuations with constant power spectral density across all times and frequencies). A third set of parameters (C_k) encapsulates underlying noise processes that are uncorrelated in time but instead are fully correlated across observing frequency, and thus it applies to simultaneously observed, multifrequency TOAs. One source for C_k is the stochastic scatter introduced from pulse "jitter" (e.g., NANOGrav Collaboration et al. 2015; Lam et al. 2017).

We used the same methodology employed by Alam et al. (2021a, 2021b) for determining the optimal values of $\{F_k, Q_k, C_k\}$ for the three narrowband data subsets listed in Table 1. For all timing solutions, we used the enterprise Bayesian pulsar timing suite (Ellis et al. 2020) for sampling the $\{F_k, Q_k, C_k\}$ terms while marginalizing over all other free parameters in the timing model. Following Alam et al. (2021b), a slightly different noise model is used in the wideband analysis. C_k cannot be modeled for wideband TOAs because there are no simultaneously observed multifrequency TOAs. However, in addition to $\{F_k, Q_k\}$ for the TOA uncertainties, analogous

error-scaling values of F_k for the DM uncertainties were also modeled. In all cases, the timing solution was refined until convergence using `tempo` by applying the noise model from the `enterprise` analysis.

We also explored the significance of temporal correlations in TOA residuals for PSR J0740+6620. Such "red" noise has been seen in other NANOGrav MSPs and is understood to reflect irregularities in pulsar spin rotation (Shannon & Cordes 2010). However, we determined that red noise is not prominent in the timing of PSR J0740+6620, as its estimation with `enterprise` yielded a Bayes significance factor of ~ 1. We therefore did not include terms that quantify red noise in the noise model for PSR J0740+6620, as NANOGrav sets a Bayes factor threshold of 100 for including red-noise parameters in timing models (e.g., NANOGrav Collaboration et al. 2015).

4. Analysis

We explored several methods for statistical analysis described below to obtain robust credible intervals on key parameters of the PSR J0740+6620 system, using the modeling procedure described in Section 3. The following analysis methods are agnostic to the use of narrowband or wideband TOAs. However, we chose to use the wideband TOAs in the work presented below given the consistency in parameters from narrowband and wideband TOAs in Table 2. Moreover, the following methods benefit from relaxed computational requirements afforded by the considerably smaller size ($\sim 1/20$) of the wideband TOA data set. The timing residuals and DM time series from the wideband data set are shown in Figure 2; a zoom-in of the overlap between the GBT and CHIME/Pulsar data sets is provided in Figure 3.

4.1. DMX Models

Table 2 presents two `tempo` models, derived from independent fits to the narrowband and wideband TOA data sets, when using the same DMX method employed by Cromartie et al. (2020). However, the different observing cadences within each TOA subset can lead to an uneven weighting of DMX estimates that impact the measurement of low-amplitude timing effects. In order to assess these impacts, we generated three sets of timing models that used slightly different DMX bins across the combined data set. Two of these DMX models used a single bin width of 3 and 6.5 days, respectively. In the third model, we used a hybrid scheme where the modeling of data acquired between MJDs 56640 and 58400 used a DMX model with bin size of 6.5 days, and all data acquired after MJD 58400 (when heightened-cadence observations began) were modeled with a DMX model using a bin size of 3 days.

These three DMX-binning choices form a small subset of possible DM variation models. Alternative methods for modeling DM variation include the Fourier decomposition of frequency-resolved TOAs as implemented in the `tempoNest` Bayesian analysis suite (Lentati et al. 2014). We nonetheless chose to use DMX, as this method is able to resolve discrete, stochastic variations in DM that cannot otherwise be adequately modeled with, for example, a Taylor expansion of the DM.

4.2. Secular Variation in the Orbital Period

All fitted timing models exhibit a significant and consistent $\dot{P}_b$. Our analysis represents the first time such variations have been detected in the PSR J0740+6620 system. Several mechanisms can yield apparent or intrinsic variations in P_b, such as those due to energy loss from quadrupole-order gravitational radiation ($(\dot{P}_b)_{GR}$; e.g., Damour & Taylor 1992), differential rotation in the Galaxy ($(\dot{P}_b)_{DR}$; e.g., Nice & Taylor 1995), off-plane acceleration in the Galactic gravitational potential ($(\dot{P}_b)_z$; Kuijken & Gilmore 1989), and apparent acceleration due to transverse motion ($(\dot{P}_b)_\mu$; Shklovskii 1970). We assumed that the total observed variation is therefore $(\dot{P}_b)_{obs} = (\dot{P}_b)_{GR} + (\dot{P}_b)_{DR} + (\dot{P}_b)_z + (\dot{P}_b)_\mu$, where

$$(\dot{P}_b)_{GR} = -\frac{192\pi}{5} \frac{(n_b T_\odot)^{5/3}}{(1 - e^2)^{7/2}} \frac{m_p m_c}{m_{tot}^{1/3}} \left(1 + \frac{73}{24}e^2 + \frac{37}{96}e^4\right), \tag{5}$$

$$(\dot{P}_b)_{DR} = -P_b \cos b \left(\frac{\Theta_0^2}{cR_0}\right)\left(\cos l + \frac{\kappa^2}{\sin^2 l + \kappa^2}\right), \tag{6}$$

$$(\dot{P}_b)_z = -1.08 \times 10^{-19} \frac{P_b}{c}$$
$$\times \left(\frac{1.25z}{[z^2 + 0.0324]^{1/2}} + 0.58z\right)\sin b, \tag{7}$$

$$(\dot{P}_b)_\mu = \frac{\mu^2 d}{c} P_b, \tag{8}$$

and where $n_b = 2\pi/P_b$ is the orbital frequency; $m_{tot} = m_p + m_c$; l and b are the Galactic longitude and latitude, respectively; Θ_0 and R_0 are the Galactocentric circular-speed and distance parameters for the solar system barycenter, respectively (e.g., Reid et al. 2014); $\kappa = (d/R_0)\cos b - \cos l$; $z = d \sin b$ is the projected vertical distance of the pulsar–binary system from the Galactic plane; and $\mu = \sqrt{\mu_\lambda^2 + \mu_\beta^2}$ is the magnitude of proper motion. In this work, we used $\Theta_0 = 236.9(4.2)$ km s^{-1} and $R_0 = 8.178(26)$[44] kpc as determined by Gravity Collaboration et al. (2019).

In Equation (7) we chose a model for quantifying the Galactic gravitational potential that is traditionally used in pulsar timing studies (Kuijken & Gilmore 1989). While other models have been developed and studied in recent pulsar literature, the $\sim 20\%$ uncertainty in $(\dot{P}_b)_{obs}$ is too large for resolving statistically meaningful differences between model predictions (Pathak & Bagchi 2018).

While expected to be negligible, we included the $(\dot{P}_b)_{GR}$ term in our analysis for completeness, as it has been observed in other pulsar–binary systems. Hu et al. (2020) presented equations for additional sources of $\dot{P}_b$ corrections that can eventually be observed through pulsar timing, arising from mechanisms such as mass loss and higher-order corrections predicted by GR. However, these additional terms are at least five orders of magnitude smaller than the current uncertainty in

---

[44] The uncertainty we report for R_0 is the composite value determined after adding the statistical and systematic uncertainties reported by Gravity Collaboration et al. (2019) in quadrature.

Table 2
Summary of Timing Parameters for PSR J0740+6620 When Using DMX to Estimate DM Values[a] in 6.5-day Bins

Parameter[b]	Narrowband TOAs	Wideband TOAs	Difference (σ_{max})[c]
Astrometry			
Ecliptic longitude, λ (deg)	103.759135333(12)	103.759135338(13)	0.4
Ecliptic latitude, β (deg)	44.102478368(13)	44.102478361(13)	0.5
Proper motion in λ, μ_λ (mas yr^{-1})	−2.735(14)	−2.737(15)	0.1
Proper motion in β, μ_β (mas yr^{-1})	−32.48(2)	−32.48(2)	0.0
Timing parallax, ϖ (mas)	1.04(18)	0.87(19)	0.9
Spin			
Spin frequency, ν_s (s^{-1})	346.5319964608338(3)	346.5319964608337(3)	0.0
Time rate of change in frequency, $\dot\nu_s$ (10^{-15} s^{-2})	−1.463874(11)	−1.463870(11)	0.4
Binary Motion			
Orbital period, P_b (days)	4.76694461933(8)	4.76694461936(8)	0.4
Projected semimajor axis, x (lt-s)	3.97755608(10)	3.97755607(11)	0.0
First Laplace-Lagrange eccentricity parameter, ϵ_1 (10^{-6})	−5.68(3)	−5.70(3)	0.7
Second Laplace-Lagrange eccentricity parameter, ϵ_2 (10^{-6})	−1.833(18)	−1.840(19)	0.3
Epoch of ascending-node passage, T_{asc}	57804.731308893(17)	57804.731308895(18)	0.1
Time rate of change in period, $\dot P_b$ (10^{-12} s s^{-1})	1.2(2)	1.2(2)	0.2
Companion mass, m_c ($M_\odot$)	0.251(5)	0.253(6)	0.3
Sine of inclination angle, $\sin i$	0.99909(12)	0.99908(13)	0.1
Profile Evolution			
First coefficient of FD expansion, c_1 (10^{-5})	−3.2(2)	n/a	n/a
Second coefficient of FD expansion, c_2 (10^{-5})	−2.0(3)	n/a	n/a
Third coefficient of FD expansion, c_3 (10^{-5})	−1.0(2)	n/a	n/a
Fit Configuration and Statistics			
Reference epoch for spin, astrometry (MJD)	57807	57807	n/a
Terrestrial clock standard	TT(BIPM2019)	TT(BIPM2019)	n/a
Solar system ephemeris	DE438	DE438	n/a
Barycentric timescale	TDB	TDB	n/a
Degrees of freedom	18,041	1,099	n/a
Goodness of fit, χ^2	18,183	1,072	n/a
Daily-averaged, weighted rms (μs)	0.27	0.28	n/a

Notes.
[a] We do not list DM values in this table owing to the large number of DMX bins used to model DM variations. We refer the reader to Figures 2 and 3 for graphical representations of the best-fit DMX data.
[b] All parameter uncertainties, listed in parentheses, denote the 68.3% (i.e., 1σ) confidence intervals in the preceding digit(s) as obtained from `tempo`.
[c] Differences between best-fit parameter estimates derived from narrowband and wideband TOAs are listed in units of the larger of the two statistical uncertainties (σ_{max}).

$\dot P_b$, and we therefore chose to ignore those terms in subsequent calculations.

Equations (5)–(8) demonstrate that $(\dot P_b)_{obs}$ is ultimately a function of m_p, m_c, and d.[45] To check for self-consistency in our best-fit timing models, we performed a Monte Carlo analysis of the relation $(P_b)_{obs}=(\dot P_b)_{GR} + (\dot P_b)_{DR} + (\dot P_b)_z + (\dot P_b)_\mu$ by sampling a set of values for $\{(\dot P_b)_{obs}, m_p, m_c, R_0, \Theta_0, \mu\}$, based on uncertainties obtained in this work or as reported in past literature, and solving for d using a Newton–Raphson method. The distribution for d obtained from a Monte Carlo simulation is shown in Figure 4, along with the probability density function (pdf) for d obtained from measurement of $\varpi = 1/d$. The overlapping pdf's demonstrate that the two independent timing effects yield statistically consistent estimates of d. The width of the pdf obtained from $\dot P_b$ is dominated

by its measurement uncertainty, and width contributions from sampling the $\{R_0, \Theta_0, \mu\}$ terms are negligible. We therefore held the $\{R_0, \Theta_0, \mu\}$ terms fixed to their best-fit values in subsequent analysis.

The pdf derived from ϖ was not corrected for the Lutz–Kelker bias in pulsar timing parallax measurements, which arises in low-precision measurements of ϖ and can lead to statistical underestimates of d (Verbiest et al. 2010). However, the consistency between the two distributions of d for PSR J0740+6620—derived from independent timing effects—indicates that the Lutz–Kelker bias is insignificant in our estimate of ϖ, and we therefore ignore this bias in subsequent analysis.

4.3. Likelihood Analysis of the Shapiro Delay and System Distance

For all timing models presented here, we used the χ^2-grid method developed by Splaver et al. (2002) for determining

---

[45] $(\dot P_b)_{obs}$ is also a function of several well-measured timing parameters, such as the orbital elements and astrometry. However, we held such values fixed to their best-fit estimates owing to their high statistical significance.
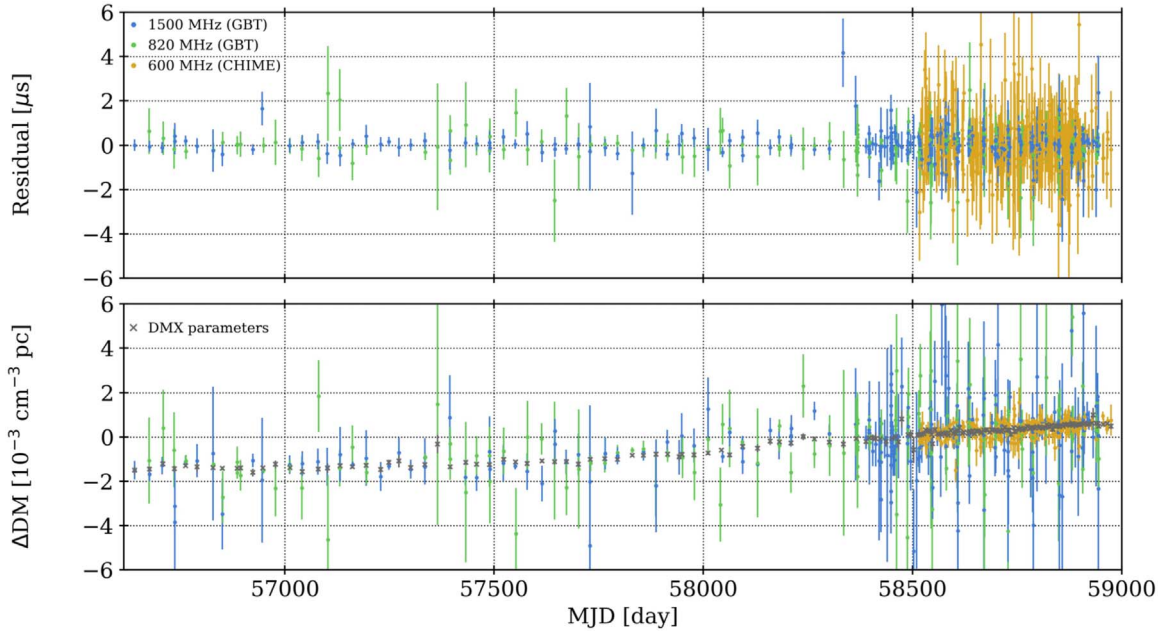
Figure 2. Timing residuals from the best-fit timing model for wideband TOAs (top), and DM time series (bottom). The colors indicate the receiver and telescope of the observation in both panels. The best-fit DMX model parameters (gray crosses) are determined by both the wideband DM measurements and the wideband TOAs. The plotted ΔDM values are offset from the nominal zero value of 14.9631 pc cm^{-3}. These wideband residual data and DMX model parameters correspond to the timing model that used the "hybrid" DMX-binning scheme discussed in Section 4.1. A zoom-in of the CHIME/Pulsar data is provided in Figure 3.

posterior pdf's and robust credible intervals for $\{m_p, m_c, i,$ and $d\}$. The procedure we used for pdf and credible-interval estimation is described as follows:

1. selected a set of values for m_c, $\cos i = \sqrt{1 - \sin^2 i}$, and d, each from uniform distributions;
2. computed values of $\sin i$, m_p, $\varpi = 1/d$, and $(\dot{P}_b)_{\text{tot}}$ using Equations (4)–(8), based on the current location in the $(m_c, \cos i, d)$ phase space;
3. held the corresponding values of $\{\varpi, m_c, \sin i, (\dot{P}_b)_{\text{tot}}\}$ fixed in the timing model;
4. refitted the timing model, allowing all timing model parameters not defined on the grid to remain unconstrained during the fit;
5. recorded the best-fit χ^2 value, and repeated the above steps for different values of $(m_c, \cos i, d)$.

We ultimately obtained a three-dimensional grid of χ^2 values computed over uniform steps in $(m_c, \cos i, d)$, which were then mapped to a likelihood function $p(\text{data, DMX}_j | m_c, \cos i, d) \propto \exp(-\Delta\chi^2/2)$, where $\Delta\chi^2 = \chi^2 - \min(\chi^2)$. The notation "DMX$_j$" refers to one of the three DMX models, labeled with subscript j, that was generated for this work. We then used Bayes's theorem to compute the posterior distribution $p(m_c, \cos i, d | \text{data, DMX}_j)$ for uniform priors on the physical parameters and choice of DMX model.

Systematic uncertainties in the (m_p, m_c, i, d) parameters may arise as a result of choices in modeling DM variations. We used Bayesian model averaging (e.g., Hoeting et al. 1999) to obtain pdf's and credible intervals that better reflect the model-independent distributions, in order to address DMX model uncertainty. The Bayesian model averaging method defines the model-independent pdf as a weighted summation of model-dependent pdf's; in the case of the three-dimensional posterior

distribution described above, the model-averaged pdf is

$$p(m_c, \cos i, d | \text{data}) = \sum_j p(m_c, \cos i, d | \text{data, DMX}_j) \times p(\text{DMX}_j | \text{data}), \quad (9)$$

where $p(\text{DMX}_j | \text{data})$ is the conditional posterior pdf for model DMX$_j$. In the absence of any preference in DMX modeling, all DMX models are equally likely and Equation (9) reduces to a straightforward averaging of the three normalized pdf's. We used Equation (9) to compute model-averaged posterior pdf's and their corresponding credible intervals for all four gridded parameters. The DMX$_j$ and model-averaged posterior pdf's for m_p are shown in Figure 5.

Posterior pdf's and credible intervals for m_p were derived from the original three-dimensional posterior pdf by noting that

$$p(m_p, \cos i, d | \text{data}) = p(m_c, \cos i, d | \text{data}) \left| \frac{\partial m_c}{\partial m_p} \right|, \quad (10)$$

$$\text{where} \frac{\partial m_c}{\partial m_p} = \frac{2 f_m m_{\text{tot}}}{3 m_c^2 \sin^3 i - 2 f_m m_{\text{tot}}}, \quad (11)$$

and where Equation (11) is determined by the Keplerian mass function (f_m). Using these original and translated pdf's, we computed credible intervals by marginalizing over the relevant subset of parameters, and we also calculated two-dimensional posterior pdf's for all possible parameter pairs. We ignored the uncertainty in f_m for all pdf calculations owing to its negligible contribution to pdf widths (relative uncertainty $\sim 10^{-7}$; Cromartie et al. 2020). Table 3 lists the credible intervals obtained using the methods described above.
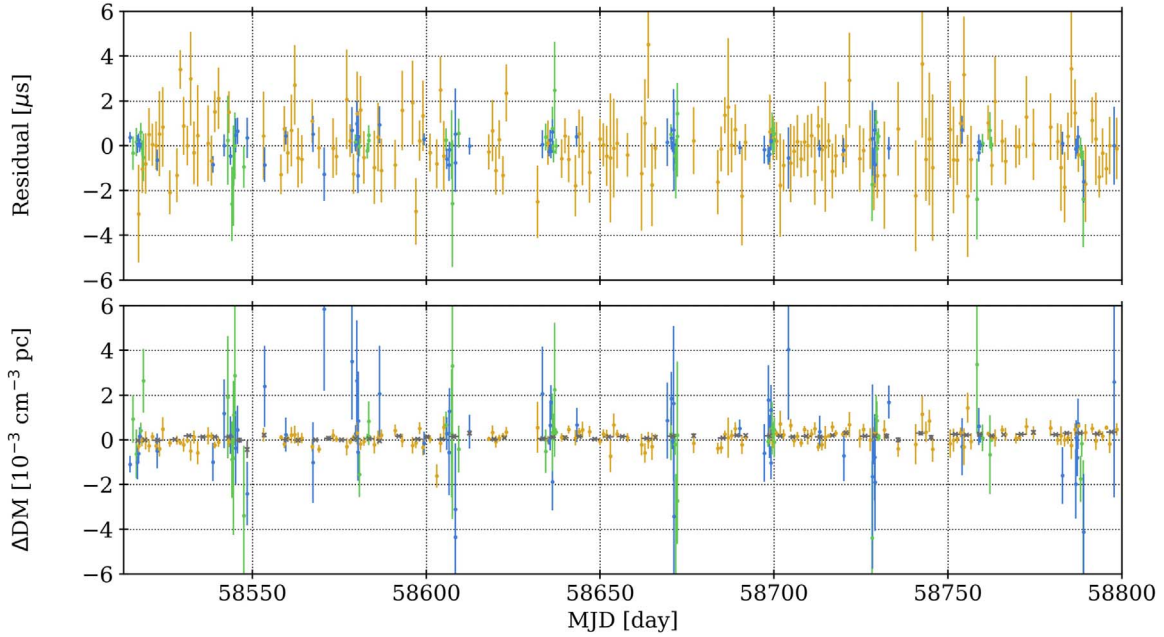
Figure 3. A zoomed-in view of the ∼1 yr overlap of GBT and CHIME/Pulsar data from Figure 2, sharing the same legend. Worthy of note are the relative cadences of observation; the smooth, shallow, and linear trend in DM over time; and the statistical weight of CHIME/Pulsar DM measurements as compared to its TOAs, relative to the GBT measurements.
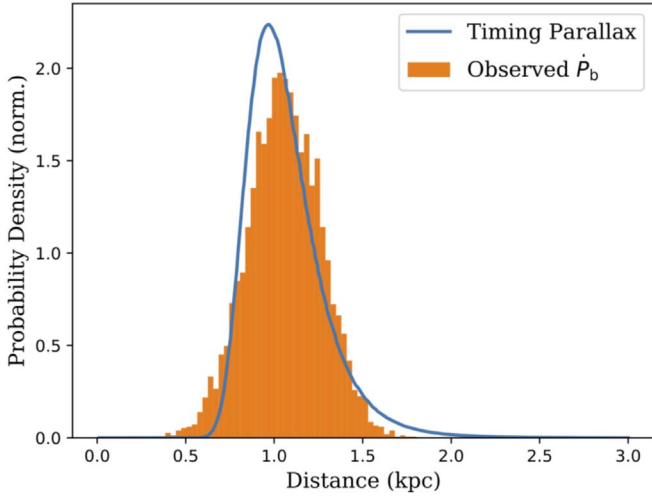
Figure 4. Independent estimates of distance from the extended timing data set for PSR J0740+6620. Shown above are distributions of distance to the PSR J0740+6620 binary system determined from the measured timing parallax (line) and Monte Carlo calculations of $(\dot{P}_b)_{\rm obs}$.

Figure 5. A comparison of normalized posterior pdf's of $m_{\rm p}$ estimated from the χ^2-grid method applied to timing models of different DMX-binning choices (dashed lines). For reference, the resultant posterior pdf obtained using the Bayesian model averaging method described in Section 4.3 is shown as the red solid line and largely overlaps the orange dashed curve.

5. Discussion

The combined timing data set for PSR J0740+6620 contains new information on temporal and DM variations, as well as improved constraints of effects previously reported by Cromartie et al. (2020). We discuss various aspects of these features in detail below, using data products generated with the techniques outlined in Section 4. These data products are publicly available and include an initial set of posterior pdf estimates used by NICER to inform their modeling of surface thermal emission with our improved estimates for the PSR J0740+6620 system parameters (Fonseca et al. 2021). Our updated constraints on mass, geometric, and distance parameters were used by NICER to constrain the radius of PSR

J0740+6620; their application is described elsewhere (Miller et al. 2021; Raaijmakers et al. 2021; Riley et al. 2021).

5.1. Timing Properties in the CHIME/Pulsar Era

All best-fit timing models developed for this work yielded consistent weighted rms residuals: ∼0.3 μs for GBT/ 1400 MHz data, ∼0.4 μs for GBT/820 MHz data, and ∼1 μs for CHIME/Pulsar data. The factor of ∼2 difference in rms residual between CHIME/Pulsar and GBT data is consistent with the expected timing precision based on observed sensitivity of the CHIME/Pulsar system; a recent timing analysis of PSR J0645+5158, another MSP observed with the

Table 3
Credible Intervals for the Shapiro Delay and Distance Parameters in the J0740+6620 System

Parameter	Cromartie et al. (2020) [a]	DMX = 3.0	DMX = 6.5	Hybrid-DMX	Model-averaged
Pulsar mass, m_p ($M_\odot$)	$2.14^{+0.10}_{-0.09}$	$2.08^{+0.07}_{-0.07}$	$2.07^{+0.07}_{-0.06}$	$2.10^{+0.07}_{-0.07}$	$2.08^{+0.07}_{-0.07}$
Companion mass, m_c ($M_\odot$)	$0.260^{+0.008}_{-0.007}$	$0.253^{+0.006}_{-0.005}$	$0.252^{+0.005}_{-0.005}$	$0.254^{+0.006}_{-0.006}$	$0.253^{+0.006}_{-0.005}$
System inclination, i (deg)	$87.38^{+0.2}_{-0.2}$	$87.53^{+0.17}_{-0.18}$	$87.61^{+0.16}_{-0.16}$	$87.53^{+0.17}_{-0.18}$	$87.56^{+0.17}_{-0.18}$
Distance, d (kpc)	$<4.4^{b}$	$1.16^{+0.17}_{-0.15}$	$1.11^{+0.17}_{-0.15}$	$1.15^{+0.17}_{-0.15}$	$1.14^{+0.17}_{-0.15}$

Notes.
[a] Values initially determined by Cromartie et al. (2020) are listed for comparison. The χ^2 gridding procedure used by Cromartie et al. (2020) only considered one DMX model, with maximum bin size of 6.5 days.
[b] Neither $\dot{P}_b$ nor timing parallax—and thus the distance—was significantly constrained with the data set presented by Cromartie et al. (2020). We instead quote here the 2σ upper limit obtained from their reported constraint.

GBT and CHIME/Pulsar, yielded similar rms statistics (CHIME/Pulsar Collaboration et al. 2020).

The white-noise model of the combined TOA set, determined using the methods outlined in Section 3.4, is consistent with the model developed by Cromartie et al. (2020). Moreover, the CHIME/Pulsar data set yields TOA uncertainty scale and quadrature values comparable to those obtained for the NANOGrav data set. Therefore, while slightly less precise than its NANOGrav counterpart, the CHIME/Pulsar instrument is producing TOAs with noise properties that are consistent with behavior observed when using other observatories.

The GBT timing data currently possess greater statistical weight on parameter constraints owing to their higher timing precision and larger number of TOAs. It is worth noting that a timing analysis of the CHIME/Pulsar data set on its own yields robust (albeit weaker) measurement of the Shapiro delay, with $m_c = 0.28(2)\,M_\odot$ and $\sin i = 0.9989(8)$ that correspond to $m_p = 2.4(3)\,M_\odot$. These CHIME/Pulsar estimates are consistent with the combined-set values obtained using the methods discussed in Section 4. The high-cadence nature of CHIME/Pulsar observations, along with the 4.8-day orbit of PSR J0740+6620, has led to a statistically significant constraint on the Shapiro delay with only ~1 yr of timing data, considerably faster than the rate that was achieved with the GBT. Nonetheless, a combination of high cadence and high sensitivity is the only way to meaningfully improve the mass and geometric estimates of the PSR J0740+6620 system. We discuss these prospects further below.

5.2. DM Variations toward PSR J0740+6620

As shown in Figure 2, the DM of PSR J0740+6620 varies smoothly and slowly across the full data set, with few outlying points and no sign of annual variations due to interactions with free electrons of the solar wind. These features are consistent with those reported by Donner et al. (2020), who analyzed a 4.8 yr data set of PSR J0740+6620 acquired using the German LOng Wavelength (GLOW) consortium of telescope stations built for the LOw Frequency ARray (LOFAR), which were all sensitive around ~150 MHz. The lack of periodic solar wind variations is expected given the high ecliptic latitude of the PSR J0740+6620 system ($\beta \approx 44°$; see Table 2), which leads to negligible traversal of the pulsar signal through the circumsolar medium.

The differences in frequency coverage and timing precision between the GBT and CHIME/Pulsar data sets lead to observable differences in their DM measurements. In particular, while the GBT data yield superior rms timing residuals

in both receiver bands than those obtained with CHIME/Pulsar, the CHIME/Pulsar data nonetheless yield better precision in DM measurements; the median uncertainty in GBT DMs determined with `PulsePortraiture` is $\sim 8 \times 10^{-4}$ pc cm^{-3}, while the same measure in the CHIME/Pulsar data set is $\sim 2 \times 10^{-4}$ pc cm^{-3}. The median DMX measurement uncertainty in the CHIME/Pulsar era has comparable precision to that obtained with GLOW by Donner et al. (2020), $\sim 4 \times 10^{-5}$ pc cm^{-3}. Further analysis of the DM time series for PSR J0740+6620 will be the subject of future works.

5.3. Updated Estimates of the Shapiro Delay Parameters

We performed the χ^2-grid and pdf analyses outlined in Section 4.3 for all three DMX timing solutions derived from the combined NANOGrav+CHIME/Pulsar data set for PSR J0740+6620. A summary of the credible intervals derived from all posterior pdf's is presented in Table 3. The model-averaged pdf's and credible intervals are shown in Figure 6.

For all four parameters defined on each χ^2 grid, the three posterior pdf's are consistent with each other at 68.3% credibility, as well as with the estimates made by Cromartie et al. (2020). Moreover, the extent of each credible interval is largely unaffected by the choice of DMX bin width. This consistency indicates that the choice of DMX model with different bin widths makes no statistical difference to the significance of our estimates in the PSR J0740+6620 system. However, it is also likely that this consistency is specific to PSR J0740+6620 owing to its slowly varying DM evolution being adequately modeled with coarser piecewise-constant DMX models.

Our 68.3% credible interval of the model-averaged $m_p = 2.08^{+0.07}_{-0.07}M_\odot$ is reduced by ~30% in comparison to the estimate made by Cromartie et al. (2020). The model-averaged m_p remains the largest of all other precisely measured pulsar masses determined with the Shapiro delay to date. The 95.4% lower bound on the model-averaged m_p, 1.95 $M_\odot$, is similar to the 1.96 $M_\odot$ lower bound initially determined by Cromartie et al. (2020). The lower limit on the maximum mass of neutron stars from the PSR J0740+6620 system therefore remains unchanged in our analysis.

The model-averaged estimate of the companion mass, $m_c = 0.253^{+0.006}_{-0.005}\,M_\odot$, remains largely consistent with the prediction from expected correlations between companion masses and orbital sizes that arise as a result of extended periods of mass transfer (Tauris & Savonije 1999). The model-averaged credible interval on m_c is in improved agreement with correlation parameters that define the $m_c - P_b$ relation for low-
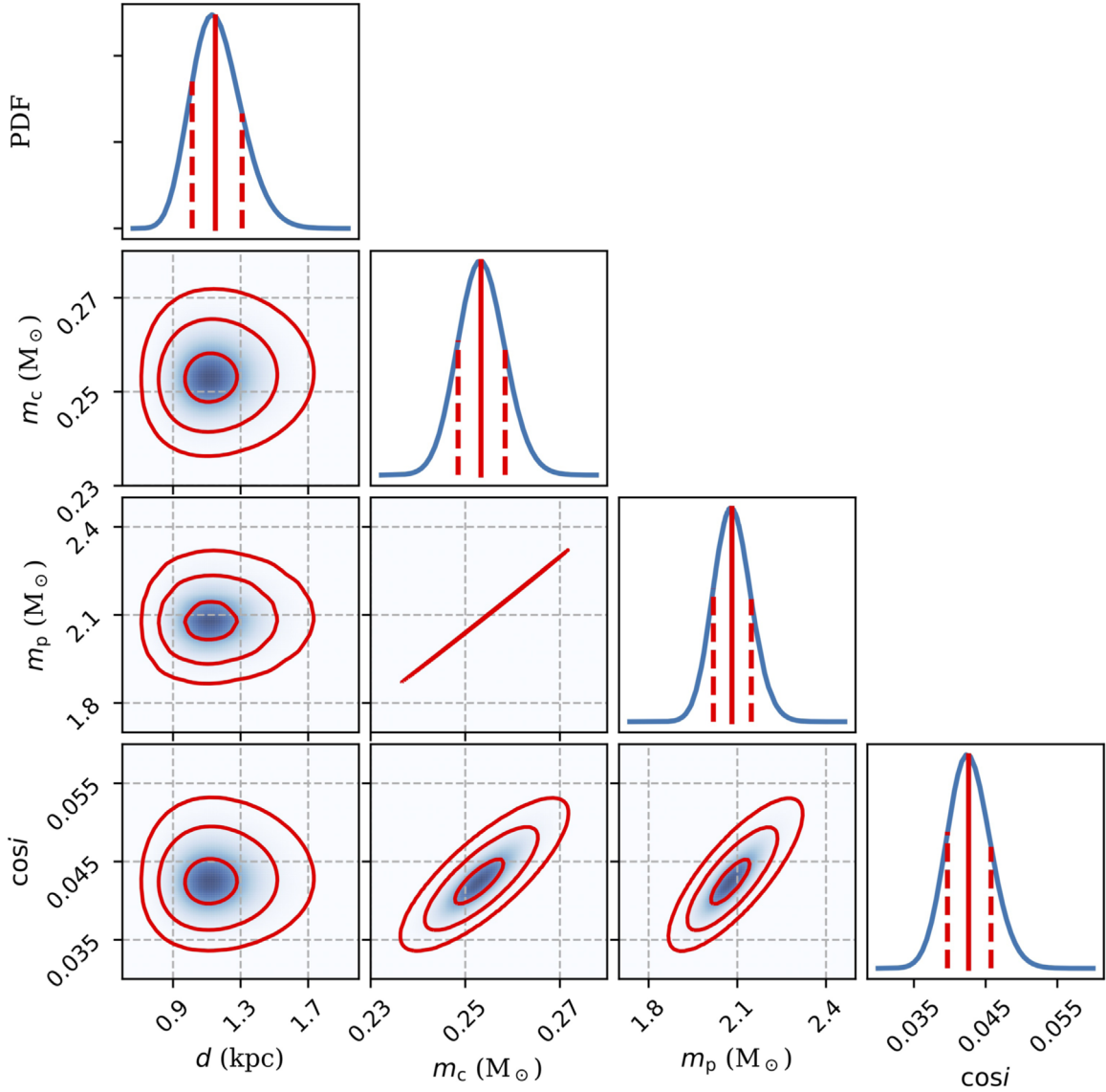
Figure 6. A triangle plot of two-dimensional, model-averaged posterior pdf's (off-diagonal) and marginalized, one-dimensional pdf's (on-diagonal) of parameters that characterize the Shapiro delay and distance to the PSR J0740+6620 system, derived using the methods outlined in Section 4.3. Vertical red lines in each diagonal panel represent the median value (solid) and 68.3% credible interval (dashed). Innermost to outermost contours denote the 68.3%, 95.4%, and 99.7% regions of credibility, respectively.

metallicity progenitors (i.e., metallic mass fraction $Z \sim 10^{-3}$ or lower), which was noted by Cromartie et al. (2020) to yield an expected $m_c \sim 0.25\,M_\odot$. Echeveste et al. (2020) demonstrated through numerical calculations that only metal-poor progenitors with helium interiors can donate matter and evolve to yield the current masses of the PSR J0740+6620 system, and our improved measurement of m_c further supports this conclusion.

5.4. Distance to the PSR J0740+6620 System

We obtained a constrained, model-averaged distance of $d = 1.14^{+0.17}_{-0.15}$ kpc from the combined NANOGrav and CHIME/Pulsar TOA data set when using the χ^2-grid method described in Section 4.3. This updated distance estimate is consistent with the distance of $d \approx 0.9$ kpc derived from the observed mean DM, placement within the Milky Way, and the model of Galactic electron number density developed by Yao et al. (2017); the distance estimated by the number density model of Cordes & Lazio (2002), $d \approx 0.6$ kpc, is less

consistent, though underlying systematic uncertainties for both electron-density models correspond to $\sim 30\%$ on d and thus reduce the tension.

Our model-averaged estimate of d is statistically consistent at the 2σ level with the marginal estimate of d derived from $\varpi = 0.5(3)$ mas made by Cromartie et al. (2020). However, these two estimates are in tension with the first estimate of $d = 0.4^{+0.2}_{-0.1}$ kpc made from initial NANOGrav timing of PSR J0740+6620 (derived from $\varpi = 2.3(6)$; Arzoumanian et al. 2018). An important distinction in these estimates is that the timing solution presented by Arzoumanian et al. (2018) yielded only a marginal detection of the Shapiro delay parameters. Arzoumanian et al. (2018) also employed an "approximate" orthometric parameterization of the Shapiro delay to model the relativistic effect as a Fourier expansion about the orbital period using a finite number of harmonic terms. As noted by Freire & Wex (2010), prominent Shapiro delays from highly inclined binary systems—as was first established for PSR J0740+6620
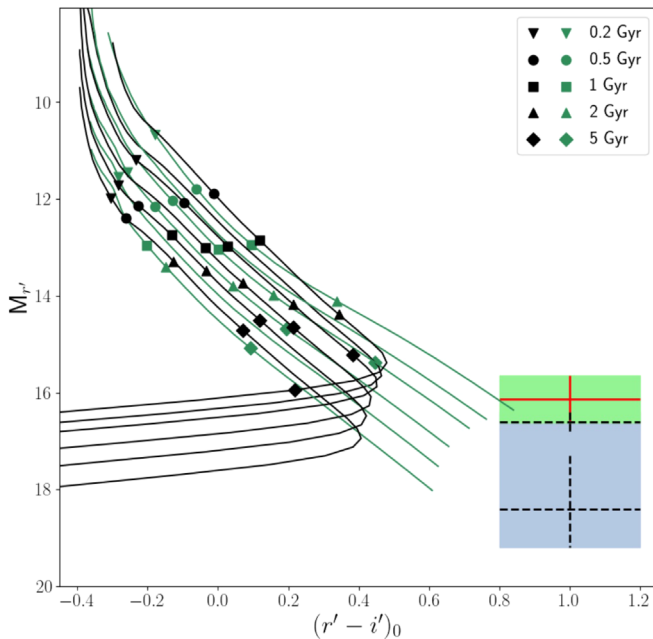
Figure 7. Color–magnitude diagram with white dwarf evolutionary sequences, evaluated at the r' and i' photometric bands. Black and green curves demonstrate the cooling predictions for white dwarfs with hydrogen and helium atmospheres, respectively (Holberg & Bergeron 2006; Kowalski & Saumon 2006; Bergeron et al. 2011; Tremblay et al. 2011). For each colored set of curves, different tracks represent masses 0.2, 0.3, 0.4, 0.6, 0.8, and 1.0 $M_\odot$, with the mass increasing from upper to lower curves. Cooling ages along each track are marked by different symbols. The position of the companion to PSR J0740+6620 is indicated by the crosses: the dashed lower and middle crosses correspond to the latest DM distance estimate $d = 0.93$ kpc and the initial timing parallax distance $d = 0.4^{+0.2}_{-0.1}$ kpc from Arzoumanian et al. (2018), respectively, and the red cross demonstrates the companion location based on the new $d = 1.14^{+0.17}_{-0.15}$ kpc. The blue shaded region shows the initial magnitude–distance uncertainty range as presented by Beronya et al. (2019), and the green shaded region indicates the new uncertainty range corresponding to $d = 1.14^{+0.17}_{-0.15}$ kpc derived in this work. The two regions slightly overlap, and the green region covers the blue one.

by Cromartie et al. (2020)—are best modeled using the analytically exact expression predicted by general relativity, instead of a finite-term Fourier expansion that is more appropriate for low-inclination systems. The combination of a sparse, low-cadence data set and suboptimal modeling likely led to an inaccurate distance estimate determined for PSR J0740+6620 by Arzoumanian et al. (2018).

Finally, we reassessed the optical properties of the white dwarf companion to PSR J0740+6620 using our direct measurement of d. Beronya et al. (2019) concluded, based on their derived magnitudes and colors of the optical counterpart and the range of contemporaneous timing parallaxes and DM-based distances, that the pulsar companion is an ultracool, helium-atmosphere white dwarf with an effective temperature <3500 K and cooling age >5 Gyr. However, Beronya et al. (2019) were not able to constrain the mass of the companion owing to the significant distance ambiguity. Observations with the Gaia satellite, designed for astrometric measurements, are currently not possible, as the r' and i' apparent magnitudes of the white dwarf companion to PSR J0740+6620 are ~26 (Beronya et al. 2019). These observed magnitudes are well above the limiting g' magnitude of ~19 for Gaia Data Release 2.[46]

Figure 7 shows a comparison of the absolute magnitude and color of the optical source with cooling predictions for white dwarfs with hydrogen and helium atmospheres, and over a range of masses[47] (Holberg & Bergeron 2006; Kowalski & Saumon 2006; Bergeron et al. 2011; Tremblay et al. 2011). The range of prior constraints on d led to a large range in absolute magnitude, shown as the blue shaded region in Figure 7, that encompasses cooling tracks of white dwarfs with 0.2–1 $M_\odot$. Our updated measurement of d restricts the absolute magnitude to the green shaded region in Figure 7, where only cooling curves for helium-atmosphere white dwarfs with masses ~0.2–0.3 $M_\odot$ remain consistent with observations. This result is in agreement with the initial estimate of m_c made by Cromartie et al. (2020) and with our updated $m_c = 0.253^{+0.006}_{-0.005} M_\odot$. The improved synergy in optical- and radio-based estimates of intrinsic parameters for the PSR J0740+6620 system favors our new measurement of d and further strengthens the counterpart association made by Beronya et al. (2019).

Future optical and infrared studies with next-generation telescopes, combined with improved distance uncertainties from radio-timing observations, will be useful for further binary evolution modeling (Echeveste et al. 2020). The increasing time span of the PSR J0740+6620 data set will further improve the measurement of $\dot{P}_b$ and thus yield a precise kinematic distance, as was recently obtained for the PSR J1909 −3744 binary system (Liu et al. 2020). Cooling predictions for white dwarfs with different composition, as well as stronger constraints on the distance and optical magnitudes, will allow for constraints on other properties of the white dwarf companion, such as its hydrogen abundance.

6. Conclusions

In this work, we extended the timing data set on the high-mass PSR J0740+6620 to incorporate additional GBT data acquired as part of the NANOGrav project and to include the initial data set being generated by CHIME/Pulsar. We generated timing solutions for PSR J0740+6620 that were derived from both narrowband and wideband arrival times collected with the GBT and CHIME/Pulsar. For each data set, we also explored using three different piecewise-constant models of DM variations to assess sensitivity of the improved mass and geometric measurements on such modeling choices.

We found that all solutions were statistically consistent with one another at 68.3% credibility, with minimal (i.e., ~1%) variation in credible intervals of the Shapiro delay parameters when comparing between several DM-evolution models. We obtained a model-averaged estimate of $m_p = 2.08^{+0.07}_{-0.07} M_\odot$, $m_c = 0.253^{+0.006}_{-0.005} M_\odot$, and $i = 87.56^{+0.17\circ}_{-0.18}$, consistent with the estimates made by Cromartie et al. (2020). Our constraint on m_p is improved by ~30%, though the lower limit we derived for the maximum mass of neutron stars remains unchanged from that determined by Cromartie et al. (2020). For the first time, our analysis also yielded a significant measurement of $\dot{P}_b$, which we argued is due to apparent acceleration from transverse motion. We found that the model-averaged $d = 1.14^{+0.17}_{-0.15}$ kpc when using the observed $\dot{P}_b$ as a constraint on the system distance, using the framework described in Section 4.

---

[46] https://www.cosmos.esa.int/web/gaia/dr2

[47] http://www.astro.umontreal.ca/~bergeron/CoolingModels

We performed an independent timing analysis of TOA data recorded with the Nançay Radio Telescope (NRT) over a 7 yr time span. All timing parameters presented in our work were statistically consistent with those estimated from NRT arrival times. The NRT data, along with forthcoming observations with the GBT and CHIME/Pulsar, will be the subject of future studies.

There are four ways in which our current estimates of the masses, geometry, and distance can be significantly improved: continued, high-cadence timing with existing facilities; observations with "ultra-wideband" radio receivers, which will become possible at the GBT in the next few years; observations with forthcoming telescopes of greater sensitivity and broad-band coverage; and measurement of additional orbital variations that can be related to one or more of the fundamental parameters considered in this work. The most promising avenue for meaningful improvement on current constraints is the use of planned next-generation facilities. Several future radio observatories—such as the Canadian Hydrogen Observatory and Radio-transient Detector (CHORD; Vanderlinde et al. 2019), 2000 dish Deep Synoptic Array (DSA-2000; Hallinan et al. 2019), and the next-generation Very Large Array (ngVLA; e.g., Chatterjee 2018)—will provide key opportunities in pulsar science with their heightened sensitivity and increased receiver bandwidths.

For pulsar timing, the radiometer equation dictates the TOA uncertainty scales as $\sigma_{\rm TOA} \propto S_{\rm sys}/\sqrt{t_{\rm obs}\Delta f}$, where $S_{\rm sys}$ is the system-equivalent flux density of the observatory, $t_{\rm obs}$ is the observation time span, and Δf is the receiver bandwidth.[48] The expected improvement of TOA precision between CHIME/Pulsar (with $S_{\rm sys} \approx 50$ Jy; CHIME/Pulsar Collaboration et al. 2020) and CHORD observations can be estimated based on current projections of CHORD design specification, with $S_{\rm sys} = 9$ Jy and $\Delta f = 1200$ MHz (Vanderlinde et al. 2019). For observations of the same $t_{\rm obs}$, the band/time-averaged TOA uncertainty obtained with CHORD is $\sigma_{\rm TOA} \sim 0.1\ \mu$s when using CHIME/Pulsar values listed in Table 1. The DSA-2000 and ngVLA have similar planned bandwidths, but a factor of ~ 5 smaller $S_{\rm sys}$ than that of CHORD. With CHORD projected to be operational by 2025, it is likely that daily TOA uncertainties of 0.1 μs and lower will be regularly achieved with next-generation observatories as soon as several years from now.

A reduction in $\sigma_{\rm TOA}$ by a factor of 10 or greater will lead to a similarly large improvement in the parameters of the Shapiro time delay. We therefore expect the credible interval of m_p to exceed values no larger than 0.01 $M_\odot$ of the median value with sufficient observations from CHORD, the DSA-2000, and/or ngVLA. The significance of $\dot{P}_b$, and thus the constraint on distance, will continue to improve such that its relative uncertainty scales as $T^{-5/2}$, where T is the data time span (Damour & Taylor 1992). With ongoing observations and future prospects, we expect to gain additional, important insight from the PSR J0740+6620 system in the near future.

ORCID iDs

E. Fonseca ⓘ https://orcid.org/0000-0001-8384-5049
H. T. Cromartie ⓘ https://orcid.org/0000-0002-6039-692X
T. T. Pennucci ⓘ https://orcid.org/0000-0001-5465-2889
P. S. Ray ⓘ https://orcid.org/0000-0002-5297-5278
A. Yu. Kirichenko ⓘ https://orcid.org/0000-0002-8139-8414
S. M. Ransom ⓘ https://orcid.org/0000-0001-5799-9714
P. B. Demorest ⓘ https://orcid.org/0000-0002-6664-965X
I. H. Stairs ⓘ https://orcid.org/0000-0001-9784-8670
L. Guillemot ⓘ https://orcid.org/0000-0002-9049-8716
A. Parthasarathy ⓘ https://orcid.org/0000-0002-4140-5616
M. Kerr ⓘ https://orcid.org/0000-0002-0893-4073
I. Cognard ⓘ https://orcid.org/0000-0002-1775-9692
P. T. Baker ⓘ https://orcid.org/0000-0003-2745-753X
H. Blumer ⓘ https://orcid.org/0000-0003-4046-884X
P. R. Brook ⓘ https://orcid.org/0000-0003-3053-6538
M. DeCesar ⓘ https://orcid.org/0000-0002-2185-1790
T. Dolch ⓘ https://orcid.org/0000-0001-8885-6388
F. A. Dong ⓘ https://orcid.org/0000-0003-4098-5222
E. C. Ferrara ⓘ https://orcid.org/0000-0001-7828-7708
W. Fiore ⓘ https://orcid.org/0000-0001-5645-5336
D. C. Good ⓘ https://orcid.org/0000-0003-1884-348X
R. Jennings ⓘ https://orcid.org/0000-0003-1082-2342
M. L. Jones ⓘ https://orcid.org/0000-0001-6607-3710
V. M. Kaspi ⓘ https://orcid.org/0000-0001-9345-0307
M. T. Lam ⓘ https://orcid.org/0000-0003-0721-651X
D. R. Lorimer ⓘ https://orcid.org/0000-0003-1301-966X
J. Luo ⓘ https://orcid.org/0000-0001-5373-5914
A. McEwen ⓘ https://orcid.org/0000-0001-5481-7559
J. W. McKee ⓘ https://orcid.org/0000-0002-2885-8485
M. A. McLaughlin ⓘ https://orcid.org/0000-0001-7697-7422
N. McMann ⓘ https://orcid.org/0000-0002-4642-1260
B. W. Meyers ⓘ https://orcid.org/0000-0001-8845-1225
A. Naidu ⓘ https://orcid.org/0000-0002-9225-9428
C. Ng ⓘ https://orcid.org/0000-0002-3616-5160
D. J. Nice ⓘ https://orcid.org/0000-0002-6709-2566
N. Pol ⓘ https://orcid.org/0000-0002-8826-1285
B. Shapiro-Albert ⓘ https://orcid.org/0000-0002-7283-1124
C. M. Tan ⓘ https://orcid.org/0000-0001-7509-0117
S. P. Tendulkar ⓘ https://orcid.org/0000-0003-2548-2926
J. K. Swiggum ⓘ https://orcid.org/0000-0002-1075-3837
H. M. Wahl ⓘ https://orcid.org/0000-0001-9678-0299
W. W. Zhu ⓘ https://orcid.org/0000-0001-5105-4058

References

Abbott, B. P., Abbott, R., Abbott, T. D., et al. 2018, PhRvL, 121, 161101
Abbott, R., Abbott, T. D., Abraham, S., et al. 2020, ApJL, 896, L44
Alam, M. F., Arzoumanian, Z., Baker, P. T., et al. 2021a, ApJS, 252, 4
Alam, M. F., Arzoumanian, Z., Baker, P. T., et al. 2021b, ApJS, 252, 5
Antoniadis, J., Freire, P. C. C., Wex, N., et al. 2013, Sci, 340, 448
Antoniadis, J., Tauris, T. M., Özel, F., et al. 2016, arXiv:arXiv:1605.01665
Arzoumanian, Z., Brazier, A., Burke-Spolaor, S., et al. 2018, ApJS, 235, 37
Backer, D. C., & Hellings, R. W. 1986, ARA&A, 24, 537
Bergeron, P., Wesemael, F., Dufour, P., et al. 2011, ApJ, 737, 28
Beronya, D. M., Karpova, A. V., Kirichenko, A. Y., et al. 2019, MNRAS, 485, 3715
Bogdanov, S., Guillot, S., Ray, P. S., et al. 2019, ApJL, 887, L25

Chatterjee, S. 2018, in ASP Conf. Ser. 517, Science with a Next Generation Very Large Array, ed. E. Murphy (San Francisco, CA: ASP), 751
CHIME/Pulsar Collaboration, Amiri, M., Bandura, K. M., et al. 2020, ApJS, in press (doi:10.3847/1538-4365/abfdcb)
Coles, W., Hobbs, G., Champion, D. J., Manchester, R. N., & Verbiest, J. P. W. 2011, MNRAS, 418, 561
Cordes, J. M., & Lazio, T. J. W. 2002, arXiv:astro-ph/0207156
Cromartie, H. T., Fonseca, E., Ransom, S. M., et al. 2020, NatAs, 4, 72
Damour, T., & Taylor, J. H. 1992, PhRvD, 45, 1840
Demorest, P. B. 2018, nanopipe: Calibration and data reduction pipeline for pulsar timing Astrophysics Source Code Library, record ascl:1803.004
Demorest, P. B., Pennucci, T., Ransom, S. M., Roberts, M. S. E., & Hessels, J. W. T. 2010, Natur, 467, 1081
Donner, J. Y., Verbiest, J. P. W., Tiburzi, C., et al. 2020, A&A, 644, A153
DuPlain, R., Ransom, S., Demorest, P., et al. 2008, Proc. SPIE, 7019, 70191D
Echeveste, R., Novarino, M. L., Benvenuto, O. G., & De Vito, M. A. 2020, MNRAS, 495, 2509
Ellis, J. A., Vallisneri, M., Taylor, S. R., & Baker, P. T. 2020, ENTERPRISE: Enhanced Numerical Toolbox Enabling a Robust PulsaR Inference SuitE, v3.0.0, Zenodo, doi:10.5281/zenodo.4059815
Fonseca, E., Cromartie, H. T., Pennucci, T. T., et al. 2021, Refined Mass and Geometric Measurements of the High-Mass PSR J0740+6620: Probability Density Functions and their Credible Intervals, Zenodo, doi:10.5281/zenodo.4773599
Freire, P. C. C., & Wex, N. 2010, MNRAS, 409, 199
Gravity Collaboration, Abuter, R., Amorim, A., et al. 2019, A&A, 625, L10
Hallinan, G., Ravi, V., Weinreb, S., et al. 2019, BAAS, 51, 255
Hoeting, J. A., M., D., Raftery, A. E., & Volinsky, C. T. 1999, StaSc, 14, 382
Holberg, J. B., & Bergeron, P. 2006, AJ, 132, 1221
Hotan, A. W., van Straten, W., & Manchester, R. N. 2004, PASA, 21, 302
Hu, H., Kramer, M., Wex, N., Champion, D. J., & Kehl, M. S. 2020, MNRAS, 497, 3118
Hunter, J. D. 2007, CSE, 9, 90
Kowalski, P. M., & Saumon, D. 2006, ApJL, 651, L137
Kuijken, K., & Gilmore, G. 1989, MNRAS, 239, 571
Lam, M. T., Cordes, J. M., Chatterjee, S., et al. 2017, ApJ, 834, 35
Lange, C., Camilo, F., Wex, N., et al. 2001, MNRAS, 326, 274
Lentati, L., Alexander, P., Hobson, M. P., et al. 2014, MNRAS, 437, 3004
Linares, M., Shahbaz, T., & Casares, J. 2018, ApJ, 859, 54
Liu, K., Desvignes, G., Cognard, I., et al. 2014, MNRAS, 443, 3752
Liu, K., Guillemot, L., Istrate, A. G., et al. 2020, MNRAS, 499, 2276
Lynch, R. S., Swiggum, J. K., Kondratiev, V. I., et al. 2018, ApJ, 859, 93
Miller, M. C., Lamb, F. K., Dittmann, A. J., et al. 2019, ApJL, 887, L24
Miller, M. C., Lamb, F. K., Dittmann, A. J., et al. 2021, ApJL, in press (doi:10.3847/2041-8213/ac089b)
NANOGrav Collaboration, Arzoumanian, Z., Brazier, A., et al. 2015, ApJ, 813, 65
Nice, D., Demorest, P., Stairs, I., et al. 2015, Tempo: Pulsar timing data analysis Astrophysics Source Code Library, record ascl:1509.002
Nice, D. J., & Taylor, J. H. 1995, ApJ, 441, 429
Özel, F., & Freire, P. 2016, ARA&A, 54, 401
Pathak, D., & Bagchi, M. 2018, ApJ, 868, 123
Pennucci, T. T. 2015, PhD thesis, Univ. Virginia
Pennucci, T. T. 2019, ApJ, 871, 34
Pennucci, T. T., Demorest, P. B., & Ransom, S. M. 2014, ApJ, 790, 93
Pennucci, T. T., Demorest, P. B., & Ransom, S. M. 2016, Pulse Portraiture: Pulsar timing, Astrophysics Source Code Library, record, ascl:1606.013
Raaijmakers, G., Greif, S. K., Riley, T. E., et al. 2020, ApJL, 893, L21
Raaijmakers, G., Riley, T. E., Watts, A. L., et al. 2019, ApJL, 887, L22
Raaijmakers, G., Greif, S. K., Hebeler, K., et al. 2021, ApJL, in press (doi:10.3847/2041-8213/ac089a)
Reid, M. J., Menten, K. M., Brunthaler, A., et al. 2014, ApJ, 783, 130
Riley, T. E., Watts, A. L., Bogdanov, S., et al. 2019, ApJL, 887, L21
Riley, T. E., Watts, A. L., Ray, P. S., et al. 2021, ApJL, in press (doi:10.3847/2041-8213/ac0a81)
Romani, R. W., Kandel, D., Filippenko, A. V., Brink, T. G., & Zheng, W. 2021, ApJL, 908, L46
Shannon, R. M., & Cordes, J. M. 2010, ApJ, 725, 1607
Shapiro, I. I. 1964, PhRvL, 13, 789
Shklovskii, I. S. 1970, SvA, 13, 562
Splaver, E. M., Nice, D. J., Arzoumanian, Z., et al. 2002, ApJ, 581, 509
Stairs, I. H. 2003, LRR, 6, 5
Tauris, T. M., & Savonije, G. J. 1999, A&A, 350, 928
Taylor, J. H. 1992, RSPTA, 341, 117
Tremblay, P.-E., Bergeron, P., & Gianninas, A. 2011, ApJ, 730, 128
Tsokaros, A., Ruiz, M., & Shapiro, S. L. 2020, ApJ, 905, 48

Vallisneri, M., & van Haasteren, R. 2017, MNRAS, 466, 4954
van Kerkwijk, M. H., Breton, R. P., & Kulkarni, S. R. 2011, ApJ, 728, 95
van Straten, W., & Bailes, M. 2011, PASA, 28, 1
Vanderlinde, K., Liu, A., Gaensler, B., et al. 2019, Canadian Long Range Plan for Astronomy and Astrophysics White Papers, Zenodo, doi:10.5281/zenodo.3765414

Verbiest, J. P. W., Lorimer, D. R., & McLaughlin, M. A. 2010, MNRAS, 405, 564
Wolff, M. T., Guillot, S., Bogdanov, S., et al. 2021, ApJL, submitted (arXiv:2105.06978)
Yao, J. M., Manchester, R. N., & Wang, N. 2017, ApJ, 835, 29